THE ASTROPHYSICAL JOURNAL, 472:275–286, 1996 November 20

THE COLD, MASSIVE MOLECULAR CLOUD G216−2.5. III. INFRARED PROPERTIES

YOUNGUNG LEE
Five College Radio Astronomy Observatory and Department of Physics and Astronomy, University of Massachusetts, Amherst, MA 01003; and Korea Astronomy Observatory, Taejon, Korea 305-348

AND

RONALD L. SNELL AND ROBERT L. DICKMAN[1]
Five College Radio Astronomy Observatory and Department of Physics and Astronomy, University of Massachusetts, Amherst, MA 01003

Received 1995 November 27; accepted 1996 June 6

ABSTRACT

We present results concerning the star-forming activities and dust properties of the unusual giant molecular cloud G216−2.5. As suggested by earlier CO observations, we confirm that this cloud is unusually cold for a GMC and shows no evidence for massive star formation. The average temperature of the dust based on the extended emission at 60 and 100 μm is 22–26 K. We attribute this low value to the lack of substantial internal heating sources. Dust heating in the cloud is probably dominated by the interstellar radiation field.

Near-infrared imaging of the *IRAS* point sources seen toward G216−2.5 reveal at least four sites of low-luminosity, and presumably low-mass, star formation within the cloud. All four sites lie preferentially toward the edge of the cloud. Two small groupings of stars are identified as the near-infrared counterparts to two of the *IRAS* point sources, and the group members may be similar to T Tauri stars. Somewhat more luminous and massive stars appear to be associated with two other *IRAS* point sources. Even the most luminous star formation site in G216−2.5 has a far-infrared luminosity of only 300 $L_\odot$.

Subject headings: infrared: ISM: continuum — ISM: clouds — ISM: individual (G216−2.5) — stars: formation

1. INTRODUCTION

G216−2.5, a cold and massive molecular cloud located in the third quadrant of the Galaxy, was discovered by Maddalena & Thaddeus (1985) and has been studied in more detail by Lee, Snell, & Dickman (1991, 1994, hereafter Papers I and II, respectively), and by Williams & Blitz (1993). While most giant molecular clouds (GMCs) are associated with strong far-infrared emission and massive star formation, Maddalena & Thaddeus (1985) found that the G216−2.5 is apparently devoid of star formation activity. Mooney (1992) found the total far-infrared luminosity from this cloud to be small and the ratio of far-infrared luminosity to cloud mass to be the smallest in the sample of GMCs he analyzed. Mooney attributed the exceptionally small luminosity to mass ratio to a result of both the absence of star formation activity and the reduced dust heating due to the marked decrease in the interstellar radiation field in the outer Galaxy.

In Paper II we suggested that G216−2.5 was a remnant cloud from a previous episode of massive star formation. This conclusion was based on a number of facts concerning the cloud, which include (i) the clear evidence of shells and rings that may be the fossil remains of earlier star formation activity, (ii) kinematics, which are dominated by a global velocity gradient, that suggests the cloud is part of a very large expanding shell, and (iii) a discrepancy between LTE and virial mass estimates that is best explained if the cloud has been severely perturbed and is currently expanding. Such a scenario is supported by the recent results of Williams & Maddalena (1995), who argue that G216−2.5 is linked to the S287 star-forming region by a large atomic hydrogen cloud. They suggest that the atomic cloud and G216−2.5 are part of a larger molecular cloud complex that has been partially photodissociated by the S287 OB stars.

In this paper we investigate more thoroughly the infrared properties of G216−2.5. We analyze both the extended far-infrared emission and the point sources detected by the *Infrared Astronomy Satellite* (*IRAS*) toward this object. The data are used to study the dust properties of the cloud and to search for embedded young stars. In addition, we have imaged the *IRAS* point sources seen toward the cloud at high angular resolution in the near-infrared *J*, *H*, and *K* bands. These images permit us to search for embedded young stars with luminosities as low as those of T Tauri stars.

2. DATA

2.1. *Far-Infrared Data*

2.1.1. *IRAS Point Sources*

A search for embedded stellar objects was made using the *IRAS* Point Source Catalog (1988). All point sources within the region mapped in CO in Paper II that were detected in at least three of the *IRAS* wavelength bands at 25, 60, and 100 μm and that had flux densities at 60 μm greater than 3 Jy were selected for study. These criteria were imposed to ensure that the sources were real and likely to be stellar in origin. Twenty sources were found that met the above criteria, and these are listed in Table 1; this table includes the *IRAS* name, galactic coordinates, and the flux densities at the four *IRAS* wavelength bands (the last two columns will be discussed in § 3.1). The ten *IRAS* point sources that lie within the boundaries of the CO emission from G216−2.5 are footnoted. The locations of the 20 point sources are

[1] Present address: National Science Foundation, Division of Astronomical Sciences, 4201 Wilson Boulevard, Arlington, VA 22230.

TABLE 1

FLUX DENSITIES AND LUMINOSITIES OF *IRAS* POINT SOURCES

Name	l	b	S_{12}	S_{25}	S_{60}	S_{100}	R	L_{FIR} ($L_\odot$)
06453−0209[a]	214.49	−1.81	1.12	6.10	22.21	36.86	1.39	189
06522−0350[a]	216.79	−1.04	1.45	3.56	23.12	69.62	1.60	300
06471−0329[a]	215.89	−2.01	1.82	6.46	15.85	23.79	1.38	129
06481−0517[a]	217.60	−2.62	1.51	7.58	20.06	32.05	1.38	168
06416−0352[a]	215.60	−3.41	0.74	1.02	10.63	26.11	1.48	115
06428−0257[a]	214.93	−2.72	1.08	1.40	17.28	38.41	1.45	174
06471−0353[a]	216.24	−2.19	0.50	0.54	7.38	26.24	1.70	112
06492−0349[a]	216.43	−1.72	0.27	0.47	9.82	30.56	1.62	131
06507−0519[a]	217.93	−2.07	0.58	0.53	8.31	31.26	1.74	133
06401−0318[a]	214.92	−3.48	0.54	0.59	10.74	36.77	1.69	158
06404−0414	215.78	−3.85	<0.25	0.24	6.67	25.47	1.74	108
06405−0356	215.53	−3.67	0.31	0.65	4.38	13.75	1.63	59
06424−0237	214.58	−2.67	0.67	0.75	4.69	13.76	1.60	60
06435−0153	214.06	−2.09	<0.25	0.47	8.80	27.00	1.62	117
06450−0619	218.18	−3.77	<0.25	0.25	5.57	16.52	1.60	72
06452−0601	217.93	−3.60	0.52	0.85	6.79	18.48	1.54	80
06486−0110	214.02	−0.61	0.48	0.54	5.88	23.50	1.78	100
06514−0424	217.19	−1.50	0.52	0.45	4.46	15.44	1.68	66
06519−0424	217.26	−1.38	0.45	0.41	6.80	39.85	2.30	191
06520−0428	217.32	−1.37	1.59	2.88	32.76	132.60	1.79	563

[a] Point source lies within the boundaries of the CO emission from G216−2.5.

shown in Figure 1, along with an outline of the CO emission.

2.1.2. *Extended Emission*

We also acquired 8° × 8° BIGMAP images to study the extended dust emission from G216−2.5. Images in all four *IRAS* wavelength bands centered on the position of G216−2.5 were obtained from the Infrared Processing and Analysis Center. All images have had a model of the zodiacal light emission removed; however, since the G216−2.5 region lies 25° out of the ecliptic plane, contamination by zodiacal emission is small in any case. A greater contamination problem is background emission from the Galaxy.

A 100 μm image of the G216−2.5 region is presented in Figure 2. The 8° × 8° area also includes two H II regions, S286 and S287. G216−2.5 is outlined by the large box in the figure, and the S287 region is outlined by the smaller dashed box. The bright emission on the eastern side of the large box at $\alpha = 06^h52^m$, $\delta = -04°28'$ originates in a more distant molecular cloud associated with S286 (Paper II).

Only the emission from the large box shown in Figure 2 will be studied in this paper. Images of the emission within this box at both 60 and 100 μm are shown in Figure 3*a* and 3*b*. (At 12 and 25 μm there appears to be little emission associated with G216−2.5, and no images are presented.)

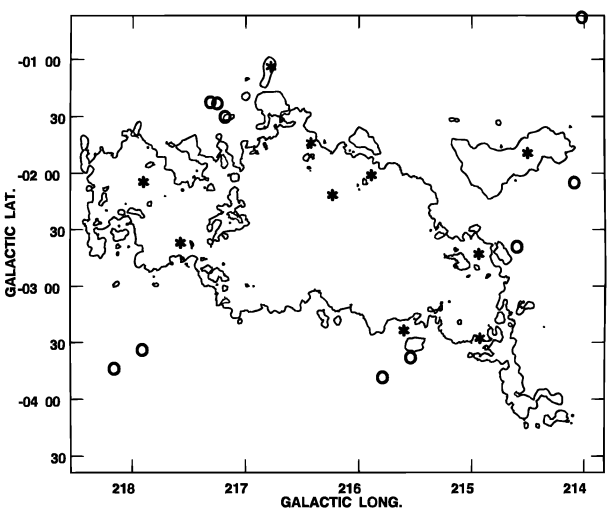

FIG. 1.—*IRAS* point sources overlain on the ^{12}CO integrated intensity map with a single contour at the 1.5 K km s^{-1} level (from Paper II). Asterisks mark the locations of the *IRAS* sources within the boundaries of G216−2.5, and open circles mark the locations of the *IRAS* sources that lie beyond the boundary of the molecular cloud.

2.2. *Near-Infrared Imaging*

The poor angular resolution of the *IRAS* observations makes the identification of individual young stars very difficult. While optical images of the *IRAS* sources with arcsecond resolution can be obtained, the high levels of visual extinction in the cloud would prevent the detection of embedded young stars. However, extinction at near-infrared wavelengths is about an order of magnitude lower than in the visible, and such observations will therefore be more sensitive to an embedded population of stars. Even at the distance of 2.2 kpc adopted for G216−2.5 (see Paper I), it is possible to detect embedded low-mass stars in the near-infrared. Accordingly, the first nine sources in Table 1 were imaged at *J*, *H*, and *K*.

Seven of the *IRAS* sources located in the main body of G216−2.5 were observed at *J*, *H*, and *K* bands with a 58 × 62 InSb array on the 1.5 m telescope at the Kitt Peak National Observatory in 1991 February. The data have an angular resolution of 1″.35 per pixel. To improve our photometric accuracy, adjacent images of the nine frames in the mosaic were overlapped by $\frac{1}{3}$ of a frame so that many of the stars would be observed more than once. The region mosaicked around each source has an angular extent roughly 3′.3 × 3′.3. In all cases, the standard star HD 40335 (Elias et al. 1982) was observed for absolute photometric calibration.

The two brightest *IRAS* sources at 100 μm were observed with the 64 × 64 element UMass HgCdTe array with a plate scale of 0″.8 per pixel on the 2.1 m telescope at Observatorio Astronomical Nacional, San Pedro Martir, Mexico in 1992 January. Mosaics were made at *K* band in a 3 × 3 frame grid centered on the *IRAS* sources. Only one frame was obtained at *J* and *H* bands centered for each *IRAS*

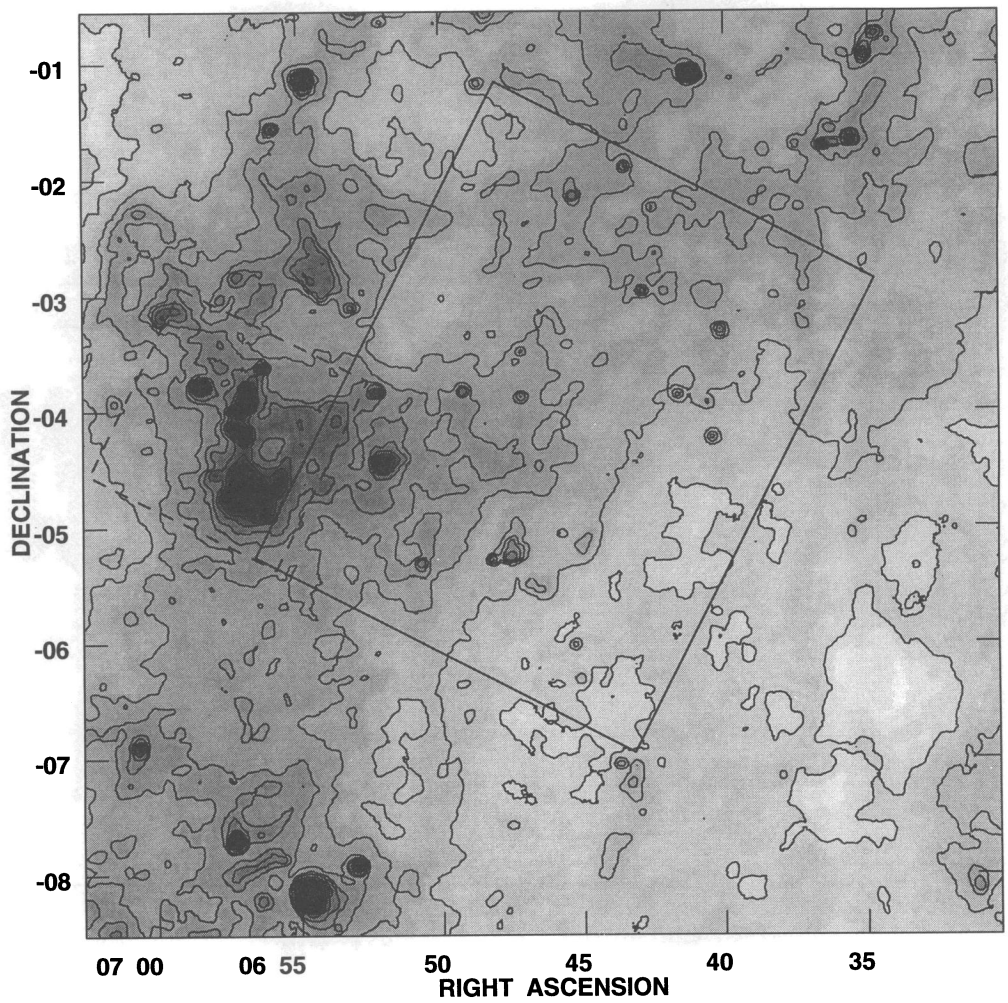

FIG. 2.—The 100 μm BIGMAP image of an 8° × 8° region centered on G216−2.5. The location of G216−2.5 is marked with the solid box. The smaller dashed area indicates the position of the S287 H II region. The lowest contour level is 10 MJy sr^{-1}, and the increment between levels is 5 MJy sr^{-1}.

source. The standard star HD 22686 (Elias et al. 1982) was observed for absolute photometric calibration.

For the Kitt Peak data, flat fields were obtained by median filtering the mosaicked frames, snd subtracting the appropriate dark current image. Median-filtered mosaic frames also served as source-free reference frames for background subtraction. Total exposure times were 60 seconds per frame at J, H, and K bands. For the San Pedro data, the J and H frames were flat-fielded and linearized by combining standard star frames, and flat fields were obtained by median filtering the mosaic frames in K band and subtracting the appropriate dark current. For the San Pedro data, exposure times were 90 s per frame in all bands.

As some fields are relatively crowded, we used the DAOPHOT package within IRAF to obtain photometry for all stars within the nine observed fields. An aperture radius of 3 pixels was used, which included most of the light from a point source at all three wavelengths. The sky background was computed from the mode of the brightness distribution in an annulus that extended from a radius of 15 pixels. The instrumental magnitudes for the standard stars (HD 40335 and HD 22686) were consistent to within 3% throughout each observing run. However, the Kitt Peak data for the sources 06416−0352, 06471−0353, and 06507−0519 were obtained when there was some haze visible, and the calibration of this data is therefore suspect. An additional source of photometric error in the Kitt Peak data is due to tracking errors. The stars in some of the images show elliptical instead of circular shapes. This made it difficult to build a good point-spread function. By iterating the process of building the point-spread function, we were able to reduce the measurement uncertainty. The typical uncertainty in the photometry was 0.1–0.2 mag in all three bands in both data sets.

The completeness limit of the photometry was estimated by computing the rms noise of the pixels within a radius of 14 pixels over an emission-free region of the sky-subtracted, flat-fielded reference field, and by assuming that the minimum detection threshold for a source is 5 σ. Based on this assumption, our detection limits are 16.0, 15.2, and 14.8 mag at J, H, and K, respectively, for the Kitt Peak data, and 16.1, 15.6, and 15.0 mag at J, H, and K, respectively, for the San Pedro Martir data.

3. FAR-INFRARED ANALYSIS

3.1. *Point Sources*

The locations of the 20 *IRAS* point sources are shown in Figure 1. In general, the sources are located somewhat randomly throughout the search box and do not appear to be concentrated toward regions of strong CO emission from the G216−2.5 molecular cloud. The only exceptions are

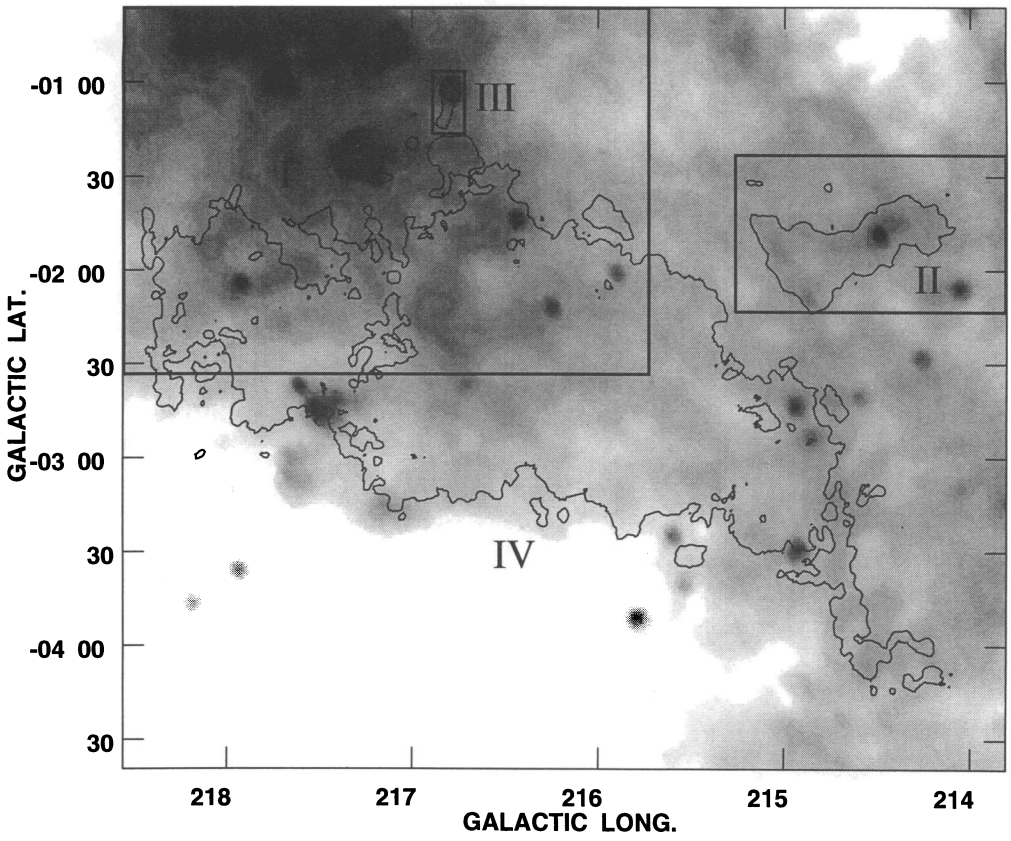

FIG. 3*a*

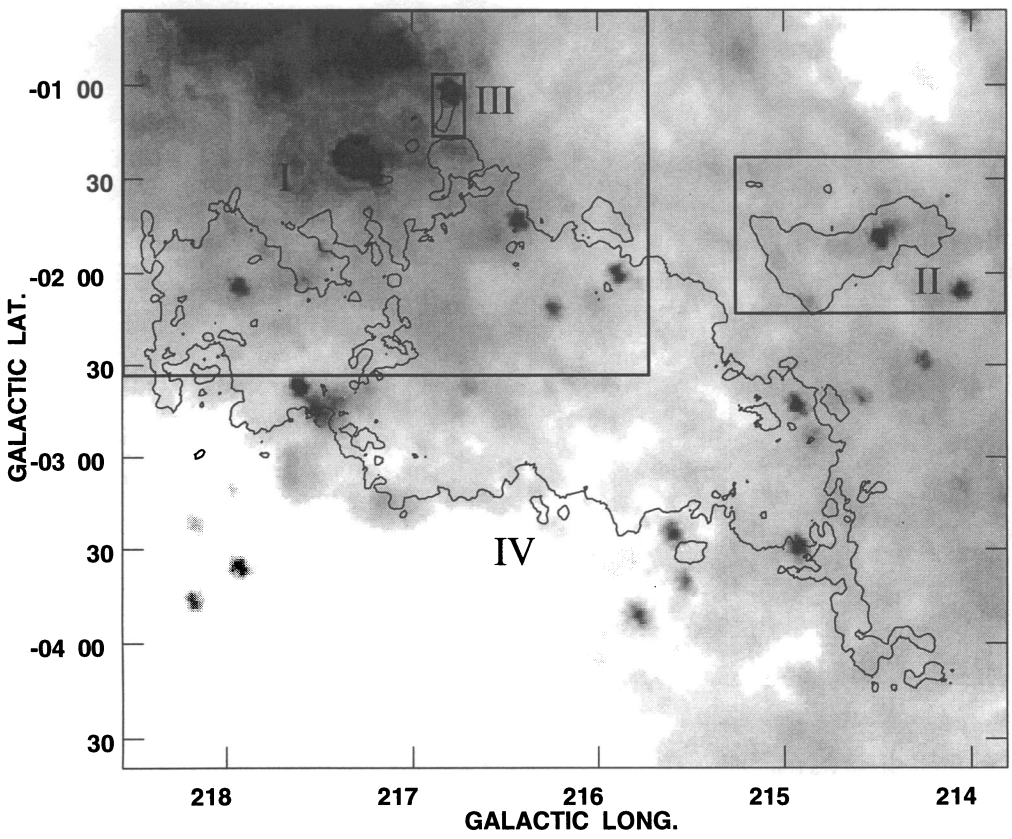

FIG. 3*b*

FIG. 3.—(*a*) The single contour represents the ^{12}CO integrated intensity at the 1.5 K km s^{-1} detection level (from Paper II). The contour map is overlain on a gray-scale image of the 100 μm intensity, where the gray scale covers the intensity range of 18–45 MJy sr^{-1}. The locations of the four regions discussed in the text are also marked. (*b*) Same as (*a*), but the contour map is overlain on a gray-scale image of the 60 μm intensity, where the gray scale covers the intensity range of 2–10 MJy sr^{-1}.

06453−0209 and 06522−0350, which are found toward the strongest CO emission in the cloud (see Paper II). If we assume all 20 of these sources to be associated with G216−2.5, and therefore to lie at a distance of 2.2 kpc, we can estimate their far-infrared luminosity according to (Lonsdale et al. 1985)

$$L_{\rm FIR} = 4\pi d^2[1.26R(1.00 \times 10^{12}S_{100} + 2.58 \times 10^{12}S_{60})] , \quad (1)$$

where S_ν is the flux density at the *IRAS* band ν, d is the distance to the object, and R is the color correction factor. The color corrections and resulting far-infrared luminosities are presented in Table 1. The most luminous source within the CO boundaries of the cloud is IRAS 06522−0350, which has a luminosity of only 300 $L_\odot$. Therefore, if any of the *IRAS* sources are actually associated with G216−2.5, their far-infrared luminosities are quite low, substantially smaller than what is expected from the massive stars usually associated with GMCs. While it is more likely that most of the sources identified are unrelated to G216−2.5 (in fact, the last three sources in Table 1 lie near the location of the background H II region S286), these data nevertheless show that G216−2.5 is relatively unique among GMCs in having no evidence for massive star formation.

A color-color diagram (S_{25}/S_{12} vs. S_{60}/S_{25}) for all the *IRAS* sources is presented in Figure 4. The filled circles in Figure 4 are the *IRAS* point sources seen toward G216−2.5, and the open circles and triangles are sources that lie outside the CO boundary of the cloud. Also included in the two-color diagram are the approximate locations of embedded core sources (*solid box*) and T Tauri stars (*dashed box*) based on the results of Harris, Clegg, & Hughes (1988), Beichman et al. (1986), and Carpenter et al. (1993). The color-color diagram suggests that four of the *IRAS* sources (06453−0209, 06522−0350, 06471−0329, and 06481−0517) have colors similar to those of embedded, core sources. Since these objects lie within the boundaries of G216−2.5, they may in fact be young stars embedded within the cloud. It is interesting that the two *IRAS* sources that lie toward the brightest CO emission in the cloud are included in these four sources. The remaining 16 sources have colors more consistent with the infrared cirrus (Weiland et al. 1986) than with known stellar objects and may therefore simply represent fluctuations in the dust density toward G216−2.5.

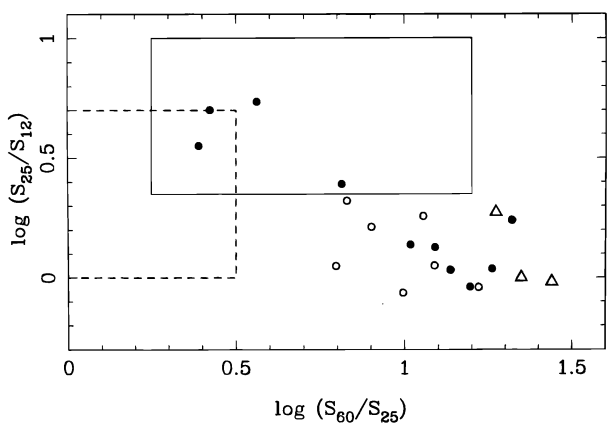

FIG. 4.—Color-color diagram for the *IRAS* point sources in the vicinity of G216−2.5. Filled symbols present *IRAS* point sources seen toward G216−2.5, and open symbols are those *IRAS* sources that lie outside the boundary of the cloud. Triangles represent those *IRAS* sources that have only upper limits on their 12 μm flux. The solid box indicates the location of embedded cores, and the dashed box indicates the location of T Tauri stars (Harris et al. 1988; Beichman et al. 1986; Carpenter et al. 1993).

3.2. *Extended Emission*

3.2.1. *Relation to CO Emission*

Since both dust and CO emission trace the mass within molecular clouds, a comparison of the two tracers may be used to constrain dust properties, such as temperature and emissivity, as well as the gas-to-dust ratio. However, to undertake such an analysis requires that the emission associated with G216−2.5 be identified. This would be straightforward if the cloud were well isolated. However, its emission is clearly contaminated by that from the more distant H II region S286 at $l = 217.^\circ3$, $b = -1.^\circ4$, and blended with the emission from the nearby cloud associated with S287 at $l = 218.^\circ1$, $b = -0.^\circ4$. Only the lower part of G216−2.5, between $b = -2.^\circ5$ and $b = -4^\circ$, is likely to be free of contamination from other sources, and it is primarily in this part of the cloud that the far-infrared emission will be studied. The far-infrared emission from the satellite cloud associated with G216−2.5 (see Paper II), centered on $l = 214.^\circ5$, $b = -1.^\circ7$, is also relatively uncontaminated.

The cloud was divided into four regions according to the degree of contamination and by spatial location; these are marked in Figures 3*a* and 3*b*. Regions I and III, which include the upper part of G216−2.5 closest to the Galactic equator and a small area of bright CO emission, are contaminated by emission from the two H II regions, S286 and S287, and ignored in the correlation analysis which follows. Region II contains the small satellite cloud, and region IV contains the lower and largely uncontaminated portion of the cloud.

In region IV a relatively good correlation is found between the far-infrared and ^{12}CO emission for values of the ^{12}CO integrated intensity above 7 K km s^{-1}. A least-squares fit between the two quantities is shown by the fitted line in Figures 5*a* and 5*b*. The equations of the fitted lines are

$$I_{100} = 0.36(\pm0.01)I_{^{12}\rm CO} + 20.41(\pm0.09) , \quad (2)$$

$$I_{60} = 0.058(\pm0.002)I_{^{12}\rm CO} + 1.55(\pm0.02) , \quad (3)$$

where the far-infrared intensity has units of MJy sr^{-1} and the CO intensity has units of K km s^{-1}. The large, nonzero intercepts most likely represent far-infrared emission from dust within the Galactic plane that is either foreground or background to G216−2.5. The intensities of the global emission from the plane inferred from the intercepts are consistent with the intensities found by Sodroski et al. (1987). We will assume that only the emission in excess of the intercept intensity is associated with G216−2.5. The intensity of the emission associated with G216−2.5 is only a small fraction of the total intensity seen at both 60 and 100 μm, which explains why the far-infrared images shown in Figures 3*a* and 3*b* do not correspond well to the molecular images. The most intense far-infrared emission in this region arises from point sources. Interestingly, this emission is not correlated with correspondingly strong CO emission; this suggests that most of the point sources are not related to the G216−2.5 cloud.

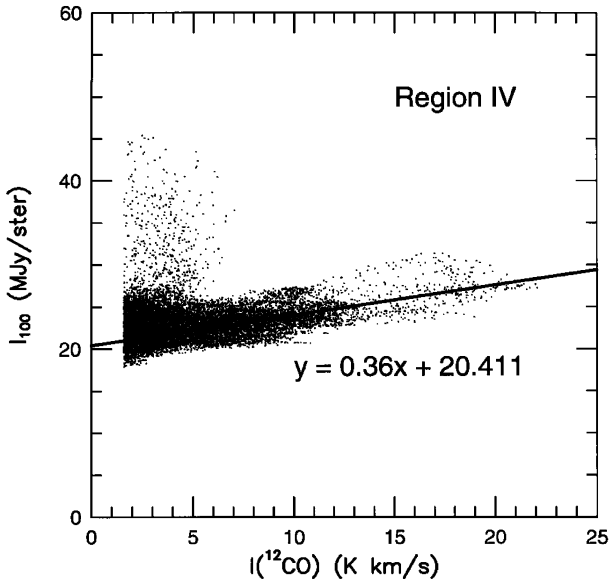

FIG. 5a

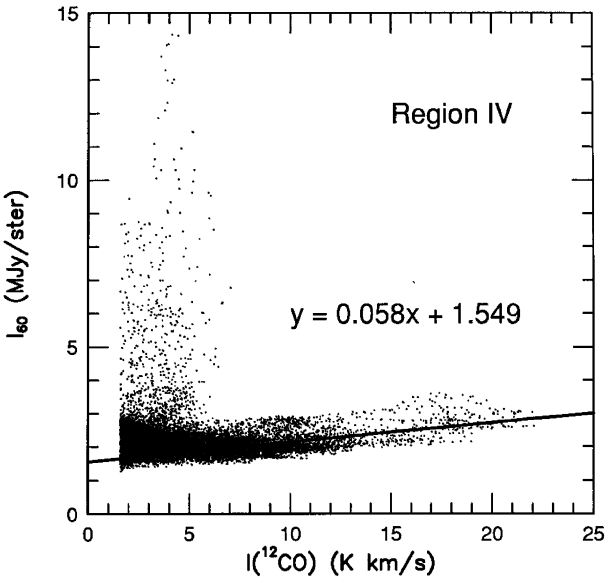

FIG. 5b

FIG. 5.—(*a*) The 100 μm intensity as a function of $I_{^{12}CO}$ for region IV. Points with $I_{^{12}CO}$ greater than 7 K km s^{-1} were fitted by a least-squares technique, and the fitted line is shown. (*b*) Same as (*a*), but for the 60 μm intensity.

The relationship between ^{12}CO integrated intensity and far-infrared intensity for region II is shown in Figures 6*a* and 6*b*. Again, a good correlation is found for most of the positions in this region. The highest far-infrared intensity is associated with the *IRAS* point source 06453−0209, and here, unlike region IV, the far-infrared intensity is strongly correlated with bright CO emission. For positions with $I_{^{12}CO} < 7$ K km s^{-1}, thus excluding *IRAS* point source 06353−0209, a least-squares fit (see Figs. 6*a* and 6*b*) gives

$$I_{100} = 0.34(\pm 0.01) I_{^{12}CO} + 24.94(\pm 0.07)\,, \quad (4)$$

$$I_{60} = 0.035(\pm 0.004) I_{^{12}CO} + 2.88(\pm 0.02)\,, \quad (5)$$

These results are similar to those found for region IV.

The slope between the far-infrared emission and CO emission associated with the point source in region II is much larger than for the bulk of the cloud (see Fig. 6). For the emission associated with the point source in region II ($I_{^{12}CO} > 7$ K km s^{-1}), the slope at 100 μm is roughly 2.7 (MJy sr^{-1}) (K km s^{-1})$^{-1}$, about 8 times steeper than for the bulk of the cloud, and at 60 μm it is roughly 1.3 (MJy sr^{-1}) (K km s^{-1}), about 36 times steeper than the rest of the cloud. This is not surprising, since the warm dust associated with the point source should produce more emission per unit column density and relatively more emission at 60 μm.

A number of authors have found linear relationships between 100 μm intensity and tracers of either the H I column density in regions of atomic gas or CO column

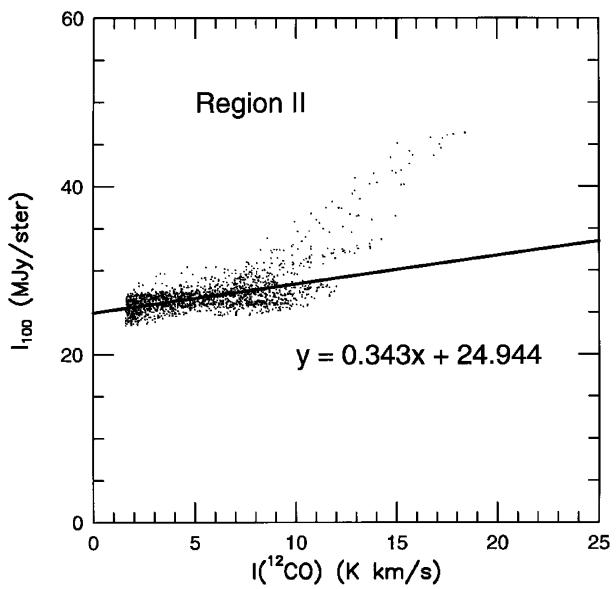

FIG. 6a

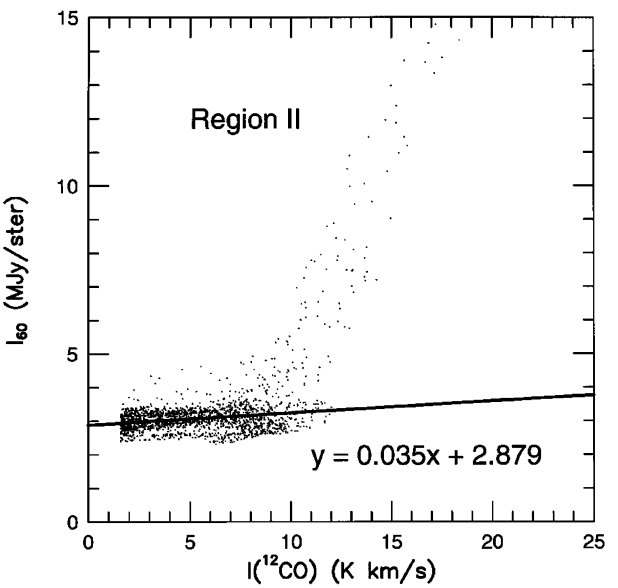

FIG. 6b

FIG. 6.—(*a*) The 100 μm intensity as a function of $I_{^{12}CO}$ for region II. Points with $I_{^{12}CO}$ less than 7 K km s^{-1} were fitted by a least-squares technique, and the fitted line is shown. The points that lie substantially above the fitted line are due to the *IRAS* point source 06453−0209. (*b*) Same as (*a*), but for the 60 μm intensity.

density in molecular clouds (Boulanger & Pérault 1988; Snell, Heyer, & Schloerb 1989). Boulanger & Pérault (1988) reported the results of a comparison of CO and far-infrared emission in nearby molecular clouds; outside regions of star formation, they reported a ratio between 100 μm intensity and CO integrated intensity in the range of 0.7–2.5 (MJy sr^{-1}) (K km s^{-1})$^{-1}$, with an average value of 1.4 (MJy sr^{-1}) (K km s^{-1})$^{-1}$. The average ratio found for G216−2.5 was 0.36 (MJy sr^{-1}) (K km s^{-1})$^{-1}$, substantially less than this value.

We can use the CO conversion factor computed from the γ-ray analysis (Bloemen 1989) of 2.3×10^{20} H$_2$ cm^{-2} (K km s^{-1})$^{-1}$ to convert the CO intensities to molecular hydrogen column densities. The ratios of far-infrared intensities to hydrogen column density in G216−2.5 are given in Table 2. These values can be compared to those found for the dark clouds B18 and HCL 2 (Snell et al. 1989) and for Orion (Boulanger & Pérault 1988) that are summarized in Table 2. The ratios found for G216−2.5 are comparable to the dark cloud ratios, and a factor of about 20 times smaller than the ratios in Orion. Snell et al. (1989) attributed the low ratios in the dark clouds to dust heated exclusively by the solar neighborhood interstellar radiation field. A similar conclusion was reached by Mooney (1992) for the clouds he classified as IR quiet. Thus, the unusually low ratios found for G216−2.5 probably results from the absence of internal or significant nearby external heating sources. If this is the case, the dust temperature should also be relatively low, as is seen in the dark clouds.

3.2.2. *Dust Temperature*

A dust color temperature can be derived from the integrated flux density ratio at 60 and 100 μm, assuming a dust emissivity law proportional to $\lambda^{-\beta}$. Since we need to include color corrections for the *IRAS* data, we use the tabulated values provided by Lonsdale et al. (1985). The emissivity index, β, is not well determined at these wavelengths, but it probably lies between $\beta = 1$ (Hildebrand 1983) and $\beta = 1.5$–2 (Cox & Mezger 1989). In G216−2.5, the mean ratio of 60 μm integrated flux density to 100 μm integrated flux density is 0.21. Assuming a dust emissivity index of $\beta = 1$, the average dust color temperature is 26 K; if the dust emissivity index is 2, then the color temperature is 22 K.

The average flux density ratio and color temperature for G216−2.5 can be compared with both star-forming GMCs and dark clouds. For star-forming clouds, the flux density ratio of 100 μm to 60 μm was found to range from 0.43 to 0.78 (Carpenter, Snell, & Schloerb 1990); the average of 0.53 corresponds to a color temperature of 37 K. A larger sample of GMCs was studied by Mooney (1992), who divided his sample into groups, IR-strong GMCs and IR-quiet GMCs, and obtained dust temperature averages of 37 K for IR-strong clouds and 31 K for IR-quiet clouds. Thus, the dust in G216−2.5 is much colder than that found in typical star-forming GMCs and even lower than the average for the IR-quiet clouds in the inner Galaxy.

The coldest dust detected by *IRAS* is often associated with nearby dark clouds, and the flux density ratios found for the two Taurus clouds, B18 and Heiles's cloud 2, are 0.17 and 0.12, respectively (Snell et al. 1989). Thus, the dust color temperature of G216−2.5 is more similar to that found in the cold dark clouds than observed even in IR-quiet GMCs.

3.2.3. *Infrared Luminosity*

We have used the fits in the previous section to define the mean intensity of the unrelated foreground and background Galactic emission in regions II and IV. After subtracting this far-infrared background, the total far-infrared flux can be estimated for the uncontaminated regions II and IV. Since there is no conspicuous star formation associated with any parts of the cloud, we assume that region I has the same emission characteristics as regions II and IV. Therefore, we have applied the same relation found between CO and far-infrared intensity for regions II and IV to estimate the far-infrared flux for region I based on its CO emission. Region III is very small, and we have ignored it. We estimate the total integrated flux density of G216−2.5 to be 4130 Jy at 100 μm and 850 Jy at 60 μm.

The total infrared luminosity $L_{\rm IR}$(tot) of the cloud is

$$L_{\rm IR}({\rm tot}) = 4\pi d^2 F_{\rm IR}({\rm tot}) , \quad (6)$$

where d is the distance to the cloud (2.2 kpc), and $F_{\rm IR}$(tot) is the total flux from 1 to 500 μm.

The flux between $\lambda = 42.4$–122.5 μm can be estimated by (Lonsdale et al. 1985)

$$F_{\rm IR} = 1.26 \times 10^{-26}(S_{100}\,\Delta\nu_{100} + S_{60}\,\Delta\nu_{60}) \quad [{\rm W\ m^{-2}}] , \quad (7)$$

where the source flux densities are in units of Janskys, and *IRAS* 60 and 100 μm bandwidths are $\Delta\nu = 2.58 \times 10^{12}$ Hz and $\Delta\nu = 1.0 \times 10^{12}$ Hz, respectively. The total far-infrared flux can then be extrapolated by assuming that the dust has a single temperature, $\overline{T_d}$. The correction factor $R(\overline{T_d}, \beta)$ for extrapolation is explicitly expressed as

$$R(\overline{T_d}, \beta) = \left(\int_{x_1}^{x_2} \frac{x^{3+\beta}}{e^x - 1}\,dx\right) \Big/ \left(\int_{x_3}^{x_4} \frac{x^{3+\beta}}{e^x - 1}\,dx\right) , \quad (8)$$

where $x_n = (hc/\lambda_n k\overline{T_d})$, $\lambda_1 = 1$ μm, $\lambda_2 = 500$ μm, $\lambda_3 = 42.5$ μm, and $\lambda_4 = 122.5$ μm, and we assume $\beta = 1$. The total far-infrared luminosity can now be expressed as

$$L_{\rm IR}({\rm tot}) = 0.394 R(\overline{T_d}, \beta)(S_{100} + 2.58 S_{60}) D^2 \quad [L_\odot] , \quad (9)$$

for D in units kpc, and with S_{100} and S_{60} in units of Janskys. Using equation (9), the estimated IR luminosity of

TABLE 2

FAR-INFRARED EMISSION–GAS COLUMN DENSITY RELATIONS

Source	$I_{100\mu m}/N$(H) [MJy sr^{-1}(10^{20} H cm^{-2})$^{-1}$]	$I_{60\mu m}/N$(H) [MJy sr^{-1}(10^{20} H cm^{-2})$^{-1}$]
G216−2.5.....	0.08	0.013
Orion	1.3	0.27
B18	0.07	0.012
HCL 2.....	0.10	0.012

G216−2.5 is $2.4 \times 10^4\ L_\odot$. The luminosity is in remarkable good agreement with that found by Mooney (1992) using a very different technique for background removal..

The LTE mass of the cloud is estimated to be $1.1 \times 10^5\ M_\odot$, considerably less than the virial mass estimate, $6.3 \times 10^5\ M_\odot$ (see Paper II). Even considering this broad range, the far-infrared luminosity-to-mass ratio of only 0.04–0.22 $L_\odot/M_\odot$ for G216−2.5 is smaller than that found for the average of the IR-quiet clouds in the study of Mooney (1992).

3.2.4. *Dust Mass*

The mass of radiating dust in G216−2.5 can be estimated using the expression given by Hildebrand (1983). Based on the integrated flux density at 100 μm, S_{100}, and the average dust temperature, T_d, the mass is

$$M_d = \frac{S_{100}\, d^2}{B(\nu, T_d)} \frac{4\langle a \rangle}{Q_{100}} \frac{\rho}{3}, \tag{10}$$

where d is the distance of the cloud, Q_{100} is the emission efficiency at 100 μm, and $B(\nu, T_d)$ is the Planck function. If it is assumed that the dust grains have a mean size $\langle a \rangle \sim 10^{-5}$ cm, a density $\rho \sim 3$ g cm^{-3}, and an emission efficiency, $Q_{100} \sim 10^{-3}$, the estimated dust mass of the cloud is then $\sim 50\ M_\odot$, about 1/2000 of the gas mass (see Paper II). This is so far below the canonical dust-to-gas ratio value (by mass) of $\sim$1/100 that as in many clouds, there must be a substantial amount of cold dust that is not emitting strongly in the *IRAS* wavelength bands.

4. NEAR-INFRARED DATA ANALYSIS

In § 3.1 we identified four *IRAS* point sources that may be relatively low-luminosity young stars or compact clusters associated with G216−2.5. To study these sources further, near-infrared images at J, H, and K bands were obtained for nine of the 10 sources that lie within the boundaries of the molecular cloud emission (the first nine sources in Table 1). If these are indeed young stellar objects in G216−2.5, we should be able to detect their near-infrared emission, and based on their colors, it may be possible to address their nature and evolutionary status (Lada & Adams 1992).

4.1. *Photometry and Images*

Near-infrared images of the four *IRAS* sources with far-infrared colors similar to embedded young stellar objects are presented in Figures 7*a*–7*d*. The data shown in Figures 7*a* and 7*b* were obtained at San Pedro Martir; the image obtained at K band is a nine-frame mosaic, while only single frames centered on the *IRAS* sources were obtained at J and H bands. The data shown in Figures 7*c* and 7*d* were obtained at Kitt Peak, and the images at each wavelength band are nine-frame mosaics. The sizes of the mosaicked fields are roughly $3' \times 3'$ for the Kitt Peak data and $2'.2 \times 2'.2$ for the San Pedro Martir data.

The near-infrared counterparts of the *IRAS* point sources, if they are young stellar objects, are expected to be relatively red (Lada & Adams 1992). In fact, extremely red objects were detected toward all four of the regions shown in Figure 7. In 06453−0209 and 06522−0350, small groupings of stars were detected toward the positions of the *IRAS* sources, many of which were so red they were detected only in the H and K band images. In 06471−0329 and 06481−0517, single red objects were detected in all three wavelength bands located toward the position of the *IRAS* sources.

Photometry at J, H, and K was performed on the nine regions observed. One hundred and fifty individual near-infrared sources were identified in the nine fields, and their magnitudes were determined. Colors were then determined only for stars brighter than $m_K \sim 14.5$ mag, $m_H \sim 15.5$ mag, and $m_J \sim 15.5$ mag. (Although the detection limit was somewhat fainter than these magnitudes, these limits were chosen to ensure accurate color determinations.)

Most of the stars detected have colors consistent with unreddened or slightly reddened main-sequence or giant stars. Since the column density of molecular material in G216−2.5 is small and there are no other significant molecular clouds along the line of sight, it is not surprising that many of the stars toward G216−2.5 show little interstellar reddening in the near-infrared. By contrast, many young stellar objects, such as T Tauri stars, Ae/Be stars, and embedded core sources have substantial excess infrared emission, presumably produced by an accretion or reprocessing disk (Lada & Adams 1992). While such excess emission can often be identified by the location of the star in a two-color diaagram ($J-H$ vs. $H-K$), not all young stellar objects can be distinguished clearly from reddened stars. Thus, without additional information, it is impossible to identify conclusively all the young stellar objects in these fields. Nevertheless, a few of the stars identified in the G216−2.5 fields do show striking infrared excesses and are coincident with the *IRAS* point sources; however, since few of these sources have detections at all three wavelength bands, we did not think it fruitful to present a two-color diagram of these sources. These are discussed in the next section.

4.2. *Description of Individual Sources*

4.2.1. *06453−0209*

IRAS 06453−0209 is located in the middle of the satellite cloud at $l = 214.5$ and $b = -1.8$ (region II) and lies toward the strongest molecular emission seen in $C^{18}O$, CS, and HCO^+ (Paper II). At the center of the K-band image presented in Figure 7*a*, five extremely red stars brighter than our adopted cutoff can be seen. Photometric data for them are presented in Table 3. Of the five, only one was detected at all three near-infrared bands, and two were detected at only K band. The one star detected in all three bands lies well outside the location of reddened and unreddened main-

TABLE 3

NEAR-INFRARED PHOTOMETRIC RESULTS

Name	$J-H$	$H-K$	m_K	A_v	M_K	M_* ($M_\odot$)
06453−0209.....	0.41	1.02	13.65	4.9	1.52	0.6
	...	0.60	13.47	4.9	1.34	0.6
	...	...	13.92	4.9	1.79	0.5
	...	0.88	13.81	4.9	1.68	0.5
	...	...	13.68	4.9	1.55	0.5
06522−0350.....	...	1.18	13.42	3.3	1.36	0.6
	...	1.81	12.24	3.3	0.18	1.1
	...	1.43	12.21	3.3	0.15	1.2
	...	1.46	13.50	3.3	1.44	0.6
	...	1.20	12.57	3.3	0.51	1.0
	...	0.63	14.17	3.3	2.11	0.4
	...	1.25	13.62	3.3	1.56	0.5
06471−0329.....	2.14	2.24	10.47	1.2	−1.50	2.8
06481−0517.....	1.22	2.14	11.31	1.2	−0.66	1.8

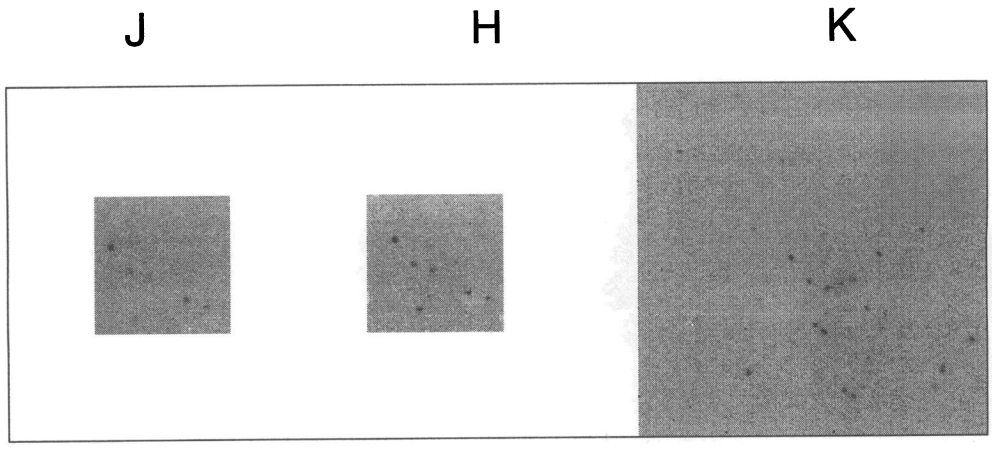

FIG. 7*a*

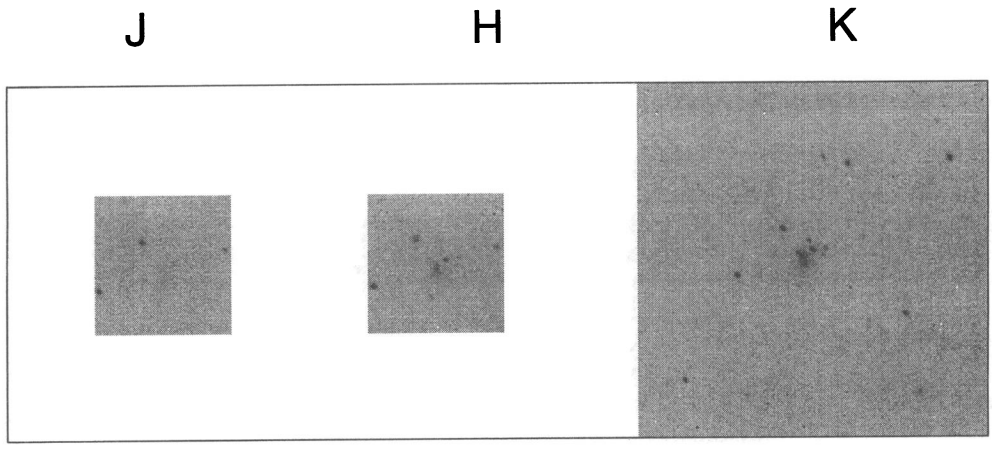

FIG. 7*b*

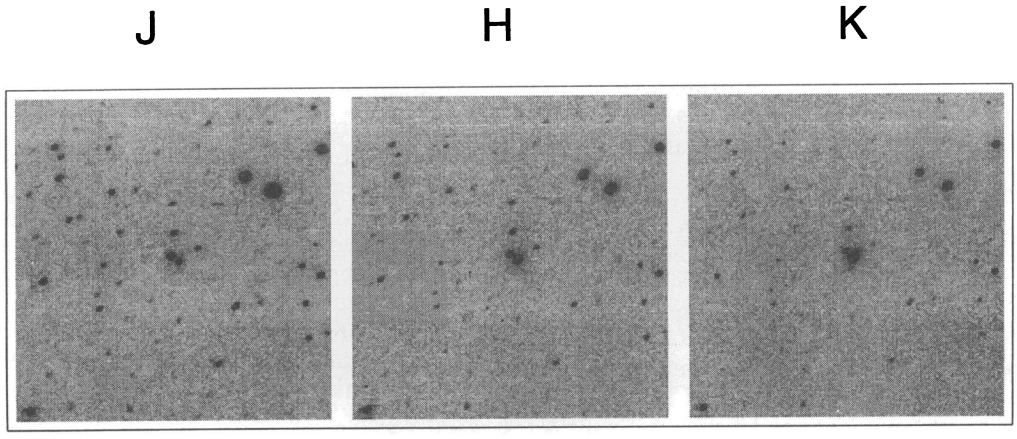

FIG. 7*c*

FIG. 7.—(*a*) The *J*-, *H*-, and *K*-band images obtained at San Pedro Martir for the region surrounding the *IRAS* point source 06453−0209. The *K*-band image is roughly 2.2 × 2.2 in size. (*b*) Same as (*a*), but for IRAS 06522−0350. (*c*) The *J*-, *H*-, and *K*-band images obtained at Kitt Peak for the region surrounding the *IRAS* source 06471−0329. The mosaicked images are approximately 3′ × 3′ in size. (*d*) Same as (*c*), but for 06481−0517.

sequence and giant stars in the $J-H$ and $H-K$ two-color diagram. Thus, it is likely that this object has a significant infrared excess.

The striking concentration of stars toward the position of an *IRAS* source that coincides with a molecular emission peak, as well as the extremely red colors, suggests strongly that the stars seen in Figure 7*a* may be physically related, young, low-luminosity objects (the total far-infrared luminosity from this region is only 189 $M_{\odot}$) that have formed recently in the satellite cloud. Fukui (1989) has detected a bipolar molecular outflow from this *IRAS* source, strengthening our interpretation further. The stars are associated with a CS core estimated in Paper II to be approximately 0.5 pc in diameter and to have a mass of 23 $M_{\odot}$.

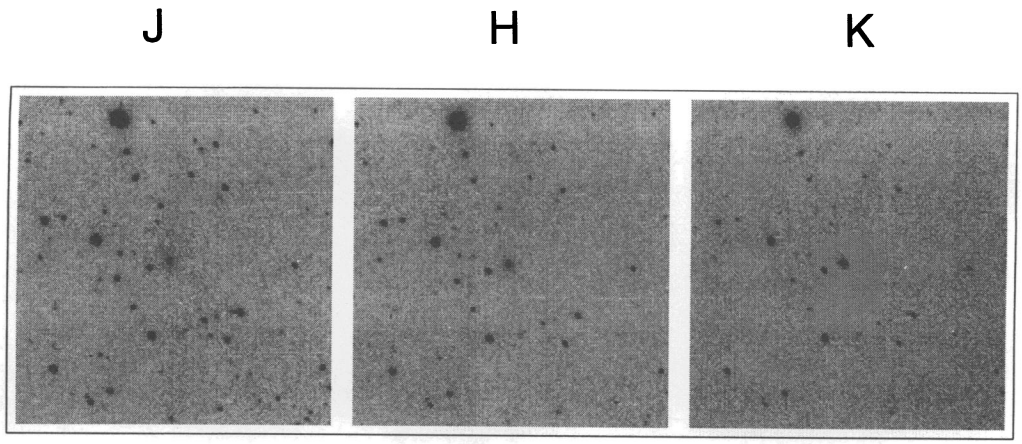

FIG. 7*d*

4.2.2. *06522−0350*

IRAS 06522−0350 is located at $l = 216.8$ and $b = -1.0$ in the very small condensation lying directly north of the main body of the cloud (region III). The strongest ^{12}CO emission in G216−2.5 is found in this direction ($T_R^* = 8.4$ K), and the *IRAS* source has the largest far-infrared luminosity (300 $L_\odot$) of the four *IRAS* point sources identified as potential young stellar objects. The *K*-band image shown in Figure 7*b* reveals seven very red stars located in a small cluster at the center of the image. There also appears to be some diffuse emission at *K* band associated with one of these stars. These stars were not detected in the *J*-band image and were detected only faintly at *H* band. Thus, none of these sources can be placed in the two-color diagram for analysis, and with only $H-K$ (see Table 3), it is not possible to identify their nature unambiguously. However, their concentration at the location of an *IRAS* point source coincident with a CO peak suggests strongly that they are part of a cluster of newly formed stars responsible for the observed far-infrared emission. Emission from C^{18}O, CS, and HCO$^+$ was detected toward this region as well (Paper II). The CS maps reveal a small core with a diameter of 0.3 pc and mass of approximately 10 $M_\odot$.

4.2.3. *06471−0329*

IRAS 06471−0329 is located at $l = 215.9$ and $b = -2.0$ near the CO boundary of the main body of G216−2.5, in the direction of relatively weak CO emission. The near-infrared images shown in Figure 7*c* reveal two bright stars at the center of the *K*-band image. These are detected at all three *IRAS* bands. Most of stars in this field have colors consistent with relatively small amounts of visual extinction. However, one of the bright stars at the position of the *IRAS* source is extremely red and lies well off the location of reddened stars in the color-color diagram. The object has colors (see Table 3) similar to the embedded core sources discussed in Lada & Adams (1992) and may be the source of the far-infrared emission. If this star lies at the distance of G216−2.5, its far-infrared luminosity is 129 $L_\odot$.

4.2.4. *06481−0517*

IRAS 06481−0517 is located at $l = 217.6$ and $b = -2.6$ near the lower boundary of the main cloud and has the largest S_{25} to S_{12} μm flux density ratio of the four *IRAS* point sources discussed here. Like 06471−0329, only weak CO emission is seen in this direction. The near-infrared images shown in Figure 7*d* reveal one relatively red central source. Its colors (see Table 3) indicate that it has a large near-infrared excess, similar to the star in 06471−0329. This source is very likely the origin of the far-infrared emission. The far-infrared luminosity of this source is 167 $L_\odot$ if the object lies at the distance to G216−2.5.

4.2.5. *Other Sources*

Besides the four regions discussed above, very red stars, with $H-K > 1$, were also seen toward two other *IRAS* point sources. Two stars were detected toward 06471−0353 and one toward 06507−0519. It seems very unlikely that such large $H-K$ colors are due solely to interstellar reddening. However, since these stars were only detected at *H* and *K* bands, it is impossible to ascertain whether they are related to the *IRAS* sources and are in fact young stellar objects.

4.3. *Absolute Magnitude and Mass*

To estimate the masses of the red stellar sources that we have tentatively identified as young stellar objects, we use the rough correlation between infrared brightness and mass for Ae/Be stars and T Tauri stars summarized by Carpenter et al. (1993). Since many of the most interesting sources were only detected at *K* band, we use M_K to estimate the masses of these objects. However, it should be noted that the *K*-band data are affected most by the presence of an accretion or reprocessing disk, and in such cases, the *K*-band measurement is a combination of photospheric emission and disk emission.

The distance modulus for a star with apparent and absolute magnitudes at *K* band of m_K and M_K, respectively, can be represented by

$$m_K - M_K = 5 \log d - 5 + A_K^c + A_K^0 , \qquad (11)$$

where d is the distance in pc, A_K^c is the extinction of the star caused by the surrounding cloud, and A_K^0 is the general interstellar extinction. Using Koorneef's (1983) extinction law, the relation between A_K and A_V is $A_K = 0.09 A_V$. The visual extinction can be calculated from the $N(^{13}\mathrm{CO}) - A_V$ relation obtained by using the star count technique described in Paper I.

Using the adopted distance of G216−2.5 of 2.2 kpc, the approx-

imately $A_V = 2.2$ mag, or $A_K = 0.2$ mag. Therefore, the absolute K magnitude can be expressed as

$$M_K = m_K + 5 - 5 \log d - 0.09A_V - 0.2$$
$$= m_K - 11.91 - 0.09A_V . \quad (12)$$

To correct for the cloud extinction, we have assumed the stars are, on average, located midway in the cloud, so only one-half the cloud extinction is assumed to be in the front of the stars. Even so, the extinction correction at K band is small, and the uncertainty in estimating the K-band extinction is not a dominant source of error. The absolute K magnitudes for the stars of interest are listed in Table 3 along with estimates of the visual extinction in that direction.

To assign masses to these objects, we constructed a mass-magnitude relation for young stars, using published data. Hillenbrand et al. (1992) provide mass estimates for 30 Ae/Be stars. Masses of 35 classical T Tauri stars (TTSs) and 10 weak-lined T Tauri stars (WTTSs) are given by Beckwith et al. (1990). After correcting all absolute K magnitudes for extinction (although the K-band extinction is very small for the most of the stars), the relationship between mass and absolute magnitude for T Tauri stars and Ae/Be stars shown in Figure 8 is obtained. The dashed line represents the magnitude-mass relation for main-sequence stars. As expected, the pre–main-sequence stars lie to the left of the main sequence and are more luminous for a given mass than stars on the main sequence.

There is a surprisingly good correlation between absolute K magnitude and mass, despite the fact that the stars are in different stages of pre–main-sequence evolution, and that as a result, for the same magnitude, the mass of a young star may vary by a factor of 3. A bisector fit (Isobe et al. 1990; Paper I) applied to the pre–main-sequence data yields a best-fit line,

$$\log [M(M_\odot)] = -0.24(\pm 0.01)M_K + 0.10(\pm 0.03) . \quad (13)$$

This is the solid line in Figure 8.

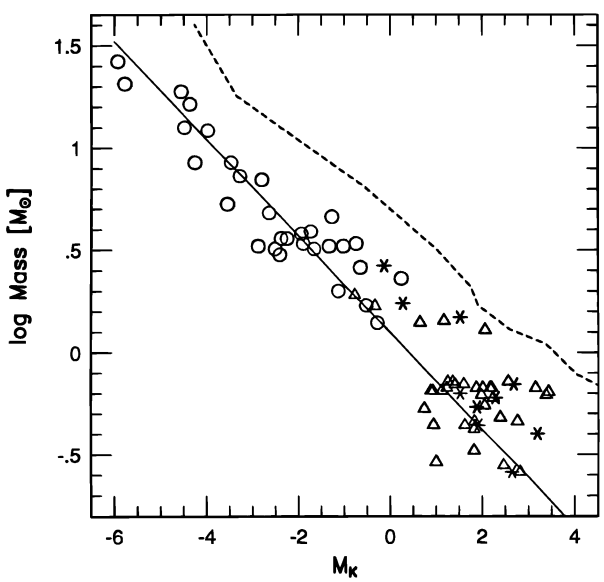

FIG. 8.—Absolute K magnitude vs. mass for various young stellar objects. Open circles are Ae/Be stars, asterisks are weak-line T Tauri stars, and open triangles are T Tauri stars. The dashed line presents the main sequence.

The masses estimated for the candidate young stellar objects are given in Table 3. The masses lie between 0.3 and 2.8 $M_\odot$ with most below 1 $M_\odot$, values similar to those found for T Tauri stars. In 06453−0209 and 06522−0350, where the evidence for the presence of young stars is the strongest, the inferred masses lie between 0.3 and 1.0 $M_\odot$. If the observed stars are responsible for the far-infrared luminosity in these regions, each would have to have a bolometric luminosity of about 40 $L_\odot$, similar to that of the most luminous T Tauri stars. However, we may not be detecting all the sources in the near-infrared contributing to the far-infrared emission; thus, the luminosity of the individual stars in each source could be substantially smaller.

5. SUMMARY

One of the unique features of G216−2.5, recognized first by Maddalena & Thaddeus (1985), is its apparent absence of massive star formation. Our analysis of both far-infrared and near-infrared emission from this cloud confirms that this truly must be the case. In Paper II we showed that the large (few parsec) and massive (100–1000 $M_\odot$) cores found in most GMCs (Goldsmith 1988) are absent in G216−2.5. However, based on our far-infrared and near infrared data, we have identified several sites of relatively low luminosity and presumably low-mass star formation within the cloud. The most interesting are associated with the *IRAS* sources 06453−0209 and 06522−0350, where we have identified small groupings of near-infrared sources that appear to coincide with relatively low mass cores. These small groupings are also associated with the brightest CO emission within the cloud. Besides these two sites, near-infrared counterparts have also been identified for the *IRAS* sources 06471−0329 and 06481−0517; both objects clearly have large infrared excesses that are likely to be due to young stellar objects forming within this cloud. All four of the *IRAS* sites are found preferentially at the boundary of the main body of G216−2.5. It is possible that this situation is related to earlier star formation episodes responsible for the shell-like morphology of the cloud.

Based on the extinction-corrected near-infrared magnitudes of the young stellar objects associated with the *IRAS* point sources, we have estimated their masses. Although these estimates are not very accurate, our results suggest that the stars in the two most prominent small groups have masses between 0.5 and 1 $M_\odot$. Thus, they may be young stellar objects similar to T Tauri stars. However, if these are the only stars contributing to the far-infrared luminosity of the *IRAS* sources, then they would have to have luminosities of order 40 $L_\odot$ each, more luminous than the average T Tauri star. The other *IRAS* sources are associated with somewhat brighter near-infrared sources; these have inferred masses between 1.8 and 2.8 $M_\odot$ and may be more similar to Ae/Be stars.

A number of other *IRAS* point sources are found toward G216−2.5. Many of these have colors similar to infrared cirrus and thus may not be stellar objects. Moreover, if they are star-forming sites within G216−2.5, we could not identify uniquely any near-infrared stellar counterparts to these sources. Even if these other *IRAS* point sources are additional young stars that have formed within the cloud, their small far-infrared luminosities suggest that they are low-mass objects.

We have also analyzed the extended far-infrared emission associated with G216−2.5. The average dust color tem-

perature inferred from this emission is 22–26 K. The far-infrared emission correlates with the gas emission, and based on the CO and far-infrared measurements, the far-infrared luminosity-to-mass ratio is only 0.04–0.22 $L_{\odot}/M_{\odot}$, much smaller than for most high-mass star-forming GMCs. Both the low dust temperature and small far-infrared luminosity-to-mass ratio are probably due to the lack of internal or nearby external heating sources. The dust heating is probably dominated by the interstellar radiation field (ISRF) and the weaker ISRF inferred by Mooney (1992) in the outer Galaxy can explain the exceptionally low dust color temperatures found in G216 − 2.5.

The Five College Radio Astronomy Observatory is operated with support from the National Science Foundation under grant AST 94-20159 and with permission of the Metropolitan District Commission of Massachusetts. We are grateful to John Carpenter for assisting in the Kitt Peak observations and to Mike Skrutskie and Mike Meyer for obtaining the data from San Pedro Martir.

REFERENCES

Beckwith, S. V. W., Sargent, A. I., Chini, R. S., & Gusten, R. 1990, AJ, 99, 924
Beichman, C. A., Myers, P. C., Emerson, J. P., Harris, S., Mathieu, R., & Jennings, R. E. 1986, ApJ, 307, 337
Bloemen, J. B. G. M. 1989, ARA&A, 27, 469
Boulanger, F., & Pérault, M. 1988, ApJ, 330, 964
Carpenter, J. M., Snell, R. L., & Schloerb, F. P. 1990, ApJ, 362, 147
Carpenter, J. M., Snell, R. L., Schloerb, F. P., & Skrutskie, M. F. 1993, ApJ, 407, 657
Cox, P., & Mezger, P. G. 1989, A&A Rev., 1, 49
Elias, J. H., Frogel, J. A., Matthews, K., & Neugebauer, G. 1982, AJ, 87, 1029
Fukui, Y. 1989, in ESO Workshop No. 33, Low Mass Star Formation and Pre-Main Sequence Objects, ed. B. Reipurth (Garching: ESO), 95
Goldsmith, P. F. 1988, in Interstellar Processes, ed. D. Hollenbach & H. Thronson (Dordrecht: Reidel), 51
Harris, S., Clegg, P., & Hughes, J. 1988, MNRAS, 235, 441
Hildebrand, R. H. 1983, QJRAS, 24, 267
Hillenbrand, L., Strom, S., Vrba, F., & Keene, J. 1992, ApJ, 397, 613
IRAS Point Source Catalog, Version 2. 1988, Joint *IRAS* Science Working Group (Washington, DC: GPO)
Isobe, T., Feigelson, E. D., Akritas, M. G., & Babu, G. J. 1990, ApJ, 364, 104
Koorneef, J. 1983, A&A, 128, 84
Lada, C. J., & Adams, F. C. 1992, ApJ, 250, 341
Lee, Y., Snell, R. L., & Dickman, R. L. 1991, ApJ, 379, 639 (Paper I)
———. 1994, ApJ, 432, 167 (Paper II)
Lonsdale, G., Helou, G., Good, J. C., & Rice, W. 1985, Catalogued Galaxies and Quasars Observed in the *IRAS* Survey (Pasadena: Jet Propulsion Laboratory)
Maddalena, R. J., & Thaddeus, P. 1985, ApJ, 294, 231
Mooney, T. 1992, Ph.D. dissertation, Univ. New York, Stony Brook
Snell, R. L., Heyer, M. H., & Schloerb, F. P. 1989, ApJ, 337, 739
Sodroski, T. J., Dwek, E., Hauser, M. G., & Kerr, F. J. 1987, ApJ, 322, 101
Weiland, J. L., Blitz, L., Dwek, E., Hauser, M. G., Magnani, L., & Rickard, L. J. 1986, ApJ, 306, L101
Williams, J. P., & Blitz, L. 1993, ApJ, 405, L75
Williams, J. P., & Maddalena, R. J. 1995, preprint